Finite Element Simulation of Wave Propagation in Periodic Piezoelectric SAW Structures

M. Hofer[1], N. Finger[2], G. Kovacs[2], J. Schöberl[3], S. Zaglmayr[3], U. Langer[3], R. Lerch[1]

Abstract— **Many surface acoustic wave (SAW) devices consist of quasiperiodic structures which are designed by successive repetition of a base cell. The precise numerical simulation of such devices including all physical effects is currently beyond the capacity of high end computation. Therewith, we have to restrict the numerical analysis to the periodic substructure. By using the finite element method (FEM), this can be done by introducing special boundaries, so called periodic boundary conditions (PBCs).**

To be able to describe the complete dispersion behavior of waves including damping effects, the PBC has to be able to model each mode which can be excited within the periodic structure. Therefore, the condition used for the PBCs must hold for each phase and amplitude difference existing at periodic boundaries. Based on the Floquet theorem, this criteria is fulfilled by our two newly developed PBC algorithms.

In the first part of this paper we describe the basic theory of the PBCs. Based on the FEM, we develop two different methods which allow the calculation of phase and attenuation constants of waves propagating on periodic structures. Further on, we show how to compute the charge distribution of periodic SAW structures with the aid of the new PBCs.

In the second part, we compare the measured and simulated dispersion behavior of waves propagating on periodic SAW structures on two different piezoelectric substrates. Finally, we compare measured and simulated input admittances of structures similar to SAW resonators.

I. Introduction

The development of SAW devices is nowadays mainly done by utilizing computer tools, because this way is much cheaper and faster compared with experimental measurements on prototypes. A very accurate method for this purpose is the finite element method (FEM) [1–6]. Therein, the real behavior of devices is modeled on the basis of partial differential equations (PDEs) which have to be discretized in time or frequency and space.

A finite element simulation of a complete SAW device is at present not possible. For example, a 3D model of a radio frequency resonator would consist of approximately 10^{10} elements, considering a necessary discretization of at least ten elements per wavelength. This amount of elements can't be handled efficiently by nowadays computers. Therefore, the models have to be reduced in complexity and size. This can be done by neglecting features which contribute only in a diminutive way to the final output or by regarding special properties of the simulated object like periodicities.

[1] The authors are with the Department of Sensor Technology, University of Erlangen-Nuremberg, Germany, e-mail: manfred.hofer@lse.e-technik.uni-erlangen.de
[2] The authors are with EPCOS AG, Munich, Germany
[3] The authors are with the Department of Computational Mathematics and Optimization, University of Linz, Austria

Many SAW devices consist of periodic structures [7, 8]. This local periodicity can be utilized to reduce the size of the FE model tremendously. The use of periodic boundary conditions (PBCs) in the FEM allows the reduction of the periodic simulation domain to one base cell. Nevertheless, the complete dispersion behavior of all waves propagating in the periodic structure can be computed.

Many publications have already been reported on the field of periodic boundary conditions, but all of them deal with the calculation of the phase constant only [9–13]. In this paper, two different methods regarding the wave propagation in periodic structures on arbitrary piezoelectric substrates are explained in detail. They allow the simulation of complete dispersion relations meaning the calculation of both, the phase and the attenuation constants. These give valuable information to SAW designers such as position of stopband edges, group and phase velocity and even reflectivity of electrodes. Further on, we show how to compute the response of periodically arranged electrodes to a harmonic voltage excitation with the aid of PBCs. Therewith, input admittances of structures similar to SAW resonators can be simulated.

The proper functionality of the two new algorithms is demonstrated by comparison of simulations with analytical results of symmetric lamb modes. The practical application of the new simulation schemes is shown by comparison of measured and simulated dispersion curves for periodic structures on two different piezoelectric substrates, 36° YX-$LiTaO_3$ and 37.5° rotated quartz, respectively. Further on, measured input admittances are compared to simulated ones and show good coincidence. All comparisons emphasize the applicability of the newly developed methods to practical tasks.

II. Periodic Boundary Condition (PBC)

SAW resonators often consist of up to thousand of electrodes. Therefore, only a negligible error is made by regarding the reflector as an infinitely extended periodic structure (see Fig. 1). The substrate - in the case of SAW devices a piezoelectric single crystal material - spreads over the lower half space ($z \leq 0$), whereas the periodic placed electrodes with arbitrary shape range from $0 \leq z \leq h$. In the upper half space, air is considered. An optional protection cover may be additionally introduced into the model. The period of the structure is the pitch p.

In every base cell (Fig. 1), a (surface-) wave impinging from the left is mainly transmitted but also partly reflected due to four main effects: a) piezoelectric shorting, b) geometric discontinuities, c) electrical regeneration and d)

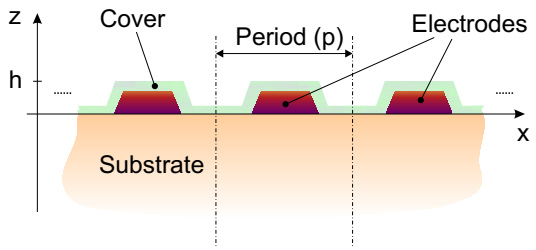

Fig. 1. Periodic SAW structure

mass loading [14]. A small part of the energy is converted into heat due to ohmic losses or conversion into bulk acoustic waves.

A. Wave Propagation in Periodic Structures

A general periodic structure can be considered as successive repetition of a base cell Ω_p (see Fig. 2). In the

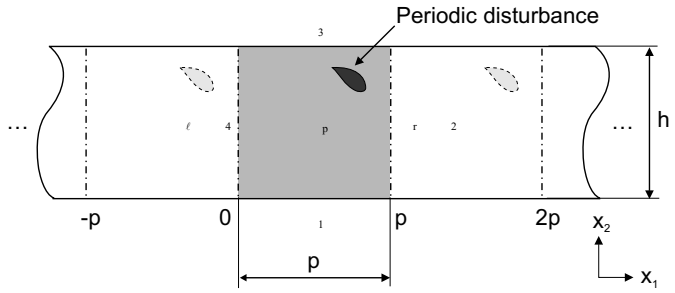

Fig. 2. Base cell Ω_p with geometric periodicity p

following, the boundary Γ_4 in Fig. 2 will be referred to as "left periodic boundary (Γ_l)" and boundary Γ_2 will be termed as "right periodic boundary", denoted by Γ_r.

The main goal of our examination is to simulate arbitrary waves propagating in periodic structures. Therefore, it is not sufficient to restrict the results to waves with wavelength λ of a fraction of twice the width p of the base cell ($\lambda = 2\,\mathrm{p}/i$ with $i \in \mathbb{N}^+$). These modes could be easily achieved by setting the degrees of freedom of the right periodic boundary Γ_r equal to those on Γ_l ($i = 2n$ with $n \in \mathbb{N}^+$), or to the negative of those from Γ_l ($i = 2n+1$ with $n \in \mathbb{N}_0$) [15, 16]. This kind of periodicity cannot be used if arbitrary waves have to be considered. Therefore, a more fundamental approach has to be pursued.

Due to the periodicity of the geometry, the resulting field distribution must be also quasi-periodic, leading to

$$u(x+p)e^{j\omega t} = u(x)e^{-\gamma p}e^{j\omega t}\,, \tag{1}$$

with u denoting the field distribution and $\gamma = \alpha + j\beta$ the complex propagation constant. The variable α describes the decay behavior and β stands for the phase propagation constant of the wave. In general, a time harmonic excitation is assumed. Therefore, the term $e^{j\omega t}$ will be omitted further on.

With a periodic function $u_p(x+p) = u_p(x)$, (1) can be written as

$$u(x) = u_p(x)e^{-\gamma p}\,. \tag{2}$$

Expanding this periodic function in a Fourier series

$$u_p(x) = \sum_{m=-\infty}^{\infty} a_m e^{-j\frac{2\pi m}{p}x} \tag{3}$$

with a_m the Fourier coefficient, the complete field distribution can be written as superposition of damped waves

$$u(x) = \sum_{m=-\infty}^{\infty} a_m e^{-\left(\gamma + j\frac{2\pi m}{p}\right)x}\,. \tag{4}$$

B. Dispersion diagram

The relation between the complex propagation constant γ and the frequency ω is needed to describe wave propagation in periodic structures. This dependency can be illustrated in a dispersion diagram (Fig. 3).

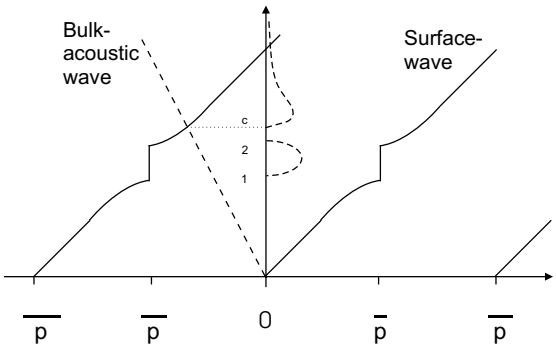

Fig. 3. Dispersion diagram of wave propagation in a periodic structure

In general, two different regions can be distinguished:

- **Wave propagation:** At frequencies below the lower stopband edge ω_1 and above the upper stopband edge ω_2 the considered modes are propagating ones. At the onset-frequency ω_c a conversion to backscattered bulk waves occurs. This results in loss of energy of the propagating wave manifesting in a nonzero, positive damping coefficient α.
- **Wave reflection:** At frequencies in the stopband ($\omega_1 < \omega < \omega_2$) the waves are reflected at periodic disturbances (e.g. electrodes). These reflections add coherently, therefore, no propagating modes exist and the waves are damped exponentially ($\alpha > 0$ at $\beta = (2n+1)\pi/p$ with $n \in \mathbb{Z}$). The width of the stopband is proportional to the reflection per disturbance [17]. If no disturbance is present, the stopband vanishes.

C. FE Formulation of the Periodic Boundary Conditions (PBCs)

The fundamental equations for the FE simulation of piezoelectric media have been published earlier. Therefore, our derivation directly starts at the algebraic system

of equations for a harmonic piezoelectric problem [18]

$$\underbrace{\begin{pmatrix} \mathbf{K}^{dd} + j\omega\mathbf{C}^{dd} - \omega^2\mathbf{M}^{dd} & \mathbf{K}^{d\phi} \\ \mathbf{K}^{\phi d} & -\mathbf{K}^{\phi\phi} \end{pmatrix}}_{\mathbf{K}} \begin{pmatrix} \mathbf{d} \\ \boldsymbol{\phi} \end{pmatrix} = \begin{pmatrix} \mathbf{F} \\ \mathbf{Q} \end{pmatrix} , \tag{5}$$

where the notation has been chosen to

$\mathbf{K}^{dd}$	mechanical stiffness matrix,
$\mathbf{C}^{dd}$	mechanical damping matrix,
$\mathbf{M}^{dd}$	mechanical mass matrix,
$\mathbf{K}^{\phi\phi}$	dielectric stiffness matrix,
$\mathbf{K}^{d\phi}$	piezoelectric coupling matrix,
$\mathbf{F}$	nodal vector of external mechanical forces,
$\mathbf{Q}$	nodal vector of electric charges,
$\mathbf{d}$	nodal vector of mechanical displacements,
$\boldsymbol{\phi}$	nodal vector of electric potentials.

For convenience, the matrix $\mathbf{K}$ is introduced as combination of all FE matrices. In further deductions, the vector of unknowns will be denoted as $\mathbf{u}$ ($\mathbf{u} = (\mathbf{d}, \boldsymbol{\phi})^T$) and the source term on the right-hand-side as $\mathbf{R}$ ($\mathbf{R} = (\mathbf{F}, \mathbf{Q})^T$). These definitions allow us to write (5) as

$$\mathbf{K}\mathbf{u} = \mathbf{R} . \tag{6}$$

D. Schur-Complement Method

To be able to incorporate the periodicity condition (1), we split the unknowns $\mathbf{u}$ into inner nodes $\mathbf{u}_i$ and boundary nodes $\mathbf{u}_b$ ($\mathbf{u}_b = (\mathbf{u}_l, \mathbf{u}_r)^T$). The same splitting is applied to the matrix $\mathbf{K}$ and the right-hand-side vector $\mathbf{R}$

$$\begin{pmatrix} \mathbf{K}_{ii} & \mathbf{K}_{ib} \\ \mathbf{K}_{bi} & \mathbf{K}_{bb} \end{pmatrix} \begin{pmatrix} \mathbf{u}_i \\ \mathbf{u}_b \end{pmatrix} = \begin{pmatrix} 0 \\ \mathbf{R}_b \end{pmatrix} . \tag{7}$$

The forces in the interior of the simulation area stay in equilibrium. Therefore, the right hand vector contributing to the inner nodes is a zero vector. This fact can be used to establish the Schur-Complement of (7) obtaining

$$\underbrace{(-\mathbf{K}_{bi}\mathbf{K}_{ii}^{-1}\mathbf{K}_{ib} + \mathbf{K}_{bb})}_{\mathbf{S}} \mathbf{u}_b = \mathbf{R}_b , \tag{8}$$

which can also be written as

$$\begin{pmatrix} \mathbf{S}_{ll} & \mathbf{S}_{lr} \\ \mathbf{S}_{rl} & \mathbf{S}_{rr} \end{pmatrix} \begin{pmatrix} \mathbf{u}_l \\ \mathbf{u}_r \end{pmatrix} = \begin{pmatrix} \mathbf{R}_l \\ \mathbf{R}_r \end{pmatrix} \tag{9}$$

with

$$\mathbf{S}_{ll} = -\mathbf{K}_{li}\mathbf{K}_{ii}^{-1}\mathbf{K}_{il} + \mathbf{K}_{ll} \tag{10}$$

$$\mathbf{S}_{lr} = -\mathbf{K}_{li}\mathbf{K}_{ii}^{-1}\mathbf{K}_{ir} + \mathbf{K}_{lr} \tag{11}$$

$$\mathbf{S}_{rl} = -\mathbf{K}_{ri}\mathbf{K}_{ii}^{-1}\mathbf{K}_{il} + \mathbf{K}_{rl} \tag{12}$$

$$\mathbf{S}_{rr} = -\mathbf{K}_{ri}\mathbf{K}_{ii}^{-1}\mathbf{K}_{ir} + \mathbf{K}_{rr} . \tag{13}$$

Due to the local support of the interpolation functions, the periodic boundaries don't couple geometrically. Hence, all entries of $\mathbf{K}_{lr}$ and $\mathbf{K}_{rl}$ are zero. Furtheron, the Schur-Complement matrices hold the following conditions

$$(\mathbf{S}_{ll} + \mathbf{S}_{rr}) = (\mathbf{S}_{ll} + \mathbf{S}_{rr})^T , \tag{14}$$

$$\mathbf{S}_{lr} = \mathbf{S}_{rl}^T . \tag{15}$$

After setting

$$\eta = e^{-\gamma p} , \tag{16}$$

the periodicity condition (1) can be incorporated by replacing $\mathbf{u}_r$ with $\eta\mathbf{u}_l$ and $\mathbf{R}_r$ with $-\eta\mathbf{R}_l$ (the minus sign is required for the equilibrium of the appearing forces on the periodic boundaries). Therewith, we arrive at

$$\begin{pmatrix} \mathbf{S}_{ll} & \mathbf{S}_{lr} \\ \mathbf{S}_{rl} & \mathbf{S}_{rr} \end{pmatrix} \begin{pmatrix} \mathbf{u}_l \\ \eta\mathbf{u}_l \end{pmatrix} = \begin{pmatrix} \mathbf{R}_l \\ -\eta\mathbf{R}_l \end{pmatrix} . \tag{17}$$

The right hand side can be eliminated by multiplying the first line with η and subsequent addition of both lines. Hence, the equation can be written as a quadratic eigenvalue problem in η

$$\eta^2\mathbf{S}_{lr}\mathbf{u}_l + \eta(\mathbf{S}_{ll} + \mathbf{S}_{rr})\mathbf{u}_l + \mathbf{S}_{rl}\mathbf{u}_l = 0 . \tag{18}$$

Therein, only the nodes on the left boundary appear. This equation can be solved, for example, by inverse iteration [19], with a two-sided Lanczos method [20], or by linearizing the system [21] which doubles the matrix size. The latter solution method is straight forward to implement and therein the standard non-symmetric eigenvalue solver from LAPACK [22] can be used.

The matrices in (18) are dense but small: the size is proportional to the number of unknowns of one periodic boundary. Due to the Schur-Complement, an inversion of the matrix $\mathbf{K}_{ii}$, which contains the unknowns of all inner nodes and is therefore of notable size, has to be performed. $\mathbf{K}_{ii}$ includes the frequency weighted mass and damping matrices and thus, the inversion has to be carried out for every frequency step separately.

E. Method with Inner Nodes (Transformation to a General Linear Eigenvalue Problem)

A different scheme can be developed by starting at (7)

$$\begin{pmatrix} \mathbf{K}_{ii} & \mathbf{K}_{il} & \mathbf{K}_{ir} \\ \mathbf{K}_{li} & \mathbf{K}_{ll} & \mathbf{K}_{lr} \\ \mathbf{K}_{ri} & \mathbf{K}_{rl} & \mathbf{K}_{rr} \end{pmatrix} \begin{pmatrix} \mathbf{u}_i \\ \mathbf{u}_l \\ \mathbf{u}_r \end{pmatrix} = \begin{pmatrix} 0 \\ \mathbf{R}_l \\ \mathbf{R}_r \end{pmatrix} , \tag{19}$$

and incorporating the periodicity condition (1) in a similar way as before in the Schur-Complement Method. This yields

$$\begin{pmatrix} \mathbf{K}_{ii} & \mathbf{K}_{il} & \mathbf{K}_{ir} \\ \mathbf{K}_{li} & \mathbf{K}_{ll} & \mathbf{K}_{lr} \\ \mathbf{K}_{ri} & \mathbf{K}_{rl} & \mathbf{K}_{rr} \end{pmatrix} \underbrace{\begin{pmatrix} \mathbf{I}_i & 0 \\ 0 & \mathbf{I}_l \\ 0 & \eta\mathbf{I}_l \end{pmatrix}}_{\mathbf{T}_1} \begin{pmatrix} \mathbf{u}_i \\ \mathbf{u}_l \end{pmatrix} = \begin{pmatrix} 0 \\ 1 \\ -\eta \end{pmatrix} \mathbf{R}_l \tag{20}$$

with $\mathbf{I}$ denoting the identity matrix. Multiplication with an appropriate matrix

$$\mathbf{T}_2 = \begin{pmatrix} \mathbf{I}_i & 0 & 0 \\ 0 & \eta\mathbf{I}_l & \mathbf{I}_l \end{pmatrix} \tag{21}$$

from the left side eliminates the right hand side. The term with the squared propagation constant η^2 cancels out because the according matrix $\mathbf{K}_{rl}$ is per definition a zero ma-

trix. Finally, the problem can be written as a general eigenvalue problem

$$\mathbf{A}\begin{pmatrix}\mathbf{u}_i\\ \mathbf{u}_l\end{pmatrix} = \eta\mathbf{B}\begin{pmatrix}\mathbf{u}_i\\ \mathbf{u}_l\end{pmatrix} \tag{22}$$

with matrices

$$\mathbf{A} = \begin{pmatrix}\mathbf{K}_{ii} & \mathbf{K}_{il}\\ \mathbf{K}_{ri} & 0\end{pmatrix} \text{ and} \tag{23}$$

$$\mathbf{B} = \begin{pmatrix}0 & -\mathbf{K}_{ir}\\ -\mathbf{K}_{li} & -(\mathbf{K}_{ll}+\mathbf{K}_{rr})\end{pmatrix}. \tag{24}$$

Compared to the Schur-Complement formulation no matrix inversion is needed. On the other hand the size of the eigenvalue problem is much larger: Here, all inner nodes and additionally the nodes on one periodic boundary contribute to the eigenvalue matrix but, fortunately, the matrices $\mathbf{A}$ and $\mathbf{B}$ keep sparse. At present, the sparsity of the matrices cannot be used due the lack of an eigenvalue solver for sparse, non-symmetric, complex matrices.

For the considered examples the Schur-Complement Method compared to the Method with Inner Nodes is approximately three times faster using the LAPACK eigenvalue solver. Beside the calculation time both methods are equal and deliver same results.

F. Solution with Defined Voltage Excitation on the Electrodes

With the above methods, all possible freely propagating modes can be calculated as eigenvalues of the described eigensystems. These give the SAW device designer valuable insight into general propagation properties of special chosen configurations and materials.

In addition to freely propagating modes (= homogeneous solutions of the system of PDEs) one is also interested in particular solutions describing the excitation properties of the system: Here, the magnitude of the electric potential on the electrodes is fixed to a predefined value. Due to the fact that the electrodes are attached to a voltage source, additional energy is supplied to the propagating waves. Therefore, the attenuation constant α may be set to zero. Assuming a phase difference of θ from unit cell to unit cell, the propagation constant takes the form $\gamma = j\beta = j\theta/p$. Since, in this case, both ω and β are given, only a simple system of linear equations has to be solved.

In principle, both methods (the Schur-Complement Method and the Method with Inner Nodes) can be applied, but the Schur-Complement needs an additional matrix inversion and therefore the Method with Inner Nodes will be utilized, resulting in

$$(\mathbf{A}-\eta\mathbf{B})\begin{pmatrix}\mathbf{u}_i\\ \mathbf{u}_l\end{pmatrix} = \begin{pmatrix}\mathbf{f}_i\\ \mathbf{f}_l\end{pmatrix}. \tag{25}$$

The vector $\mathbf{f}_l$ is a zero vector because no external forces or electric potentials can be applied to the periodic boundaries. The additional boundary conditions of the potential on the electrodes are regarded in the right hand side vector $\mathbf{f}_i$.

The evaluation of the complete result vector $(\mathbf{u}_i, \mathbf{u}_l)$ or at least the contributions of the electric voltage for every given phase difference θ and every frequency ω can hardly be managed. Therefore, the calculation of the overall electrode charge Q is performed. It can be used to compute the input admittance Y

$$Y = \frac{j\omega Q}{U} \tag{26}$$

for a given excitation voltage U and angular frequency ω. The calculation of the charge is done by using Maxwell's equation

$$\nabla\cdot\mathbf{D} = q \tag{27}$$

with $\mathbf{D}$ the dielectric displacement vector and q the electric charge density. Using Gauss theorem and regarding the piezoelectric effect, one yields

$$\int_\Gamma (\mathbf{K}^{\phi u} - \mathbf{K}^{\phi\phi})\begin{pmatrix}\mathbf{u}\\ \boldsymbol{\phi}\end{pmatrix} d\boldsymbol{\Gamma} = Q\,, \tag{28}$$

with $\boldsymbol{\Gamma}$ the vector of the integration area. If this area is chosen directly on the electrode interfaces, one additionally gets the charge distribution on the electrode (see Fig. 4).

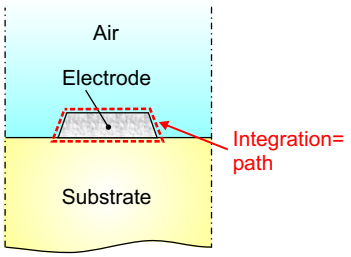

Fig. 4. Integration path for the calculation of the electrode charge distribution

G. Verification of the newly developed PBCs

The verification of the presented methods was done by comparing the analytic solution with simulated results of pure mechanical symmetric plate modes. They can be described by [23]

$$\frac{\tan k_{ts}b/2}{\tan k_{tl}b/2} = -\frac{4\beta^2 k_{tl}k_{ts}}{(k_{ts}^2-\beta^2)^2}\,, \tag{29}$$

with b denoting the plate thickness, k_{tl} the wave number of the longitudinal wave, k_{ts} the wave number of the shear wave and β the propagation constant.

The dependencies between wave numbers and propagation constant can be written as

$$k_{tl}^2 = \left(\frac{\omega}{c_L}\right)^2 - \beta^2 \text{ and} \tag{30}$$

$$k_{ts}^2 = \left(\frac{\omega}{c_S}\right)^2 - \beta^2\,, \tag{31}$$

with c_L the velocity of the longitudinal wave and c_S the velocity of the shear wave. In Fig. 5 the complex valued

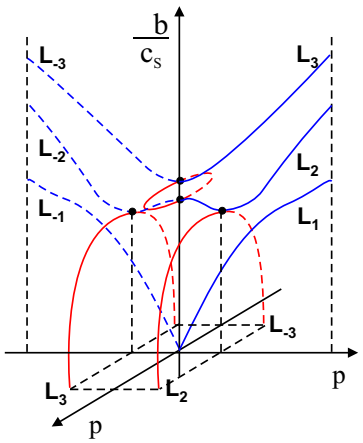

Fig. 5. Dispersion diagram of the analytical solution of three lamb waves of lowest order (after Mindlin: see [23])

analytic solution of the three lamb waves of lowest order is displayed.

The FE model for the simulation of symmetric plate modes can be seen in Fig. 6. Therein, p denotes the

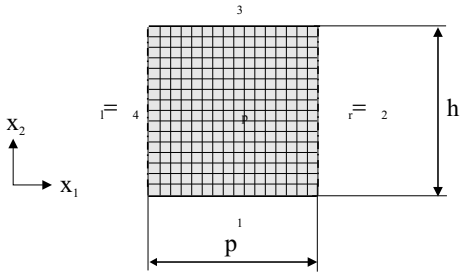

Fig. 6. FE model for calculation of plate modes

width of the base cell and h is the half plate thickness, due to a symmetry boundary condition on Γ_1. The boundaries denoted with Γ_l and Γ_r are the left and right periodic boundary. On Γ_1 displacements in x_2 direction have been suppressed to receive only symmetric lamb modes. On Γ_3 a force free boundary is assumed.

The calculation was performed on the basis of the two methods introduced above. Both methods deliver similar results. The Schur-Complement Method was approximately three times faster, because the used LAPACK eigenvalue solver could handle only dense matrices. A comparison of analytic (Fig. 5) and simulated results (Fig. 7) shows a good qualitative congruence. Both, the phase and the attenuation constant coincide very well.

A quantitative comparison can be seen in Fig. 8. Therein, the values of simulated and analytical modes match very good for small phase constants β. Looking at higher values of β, one can discover little differences which can be explained by the discretization: If the phase constant increases, the wave length gets smaller and, therefore, with a constant discretization of the simulation domain, the amount of elements per wavelength decreases. Hence, the geometric resolution of the FE grid at higher β values is not as good as at low values.

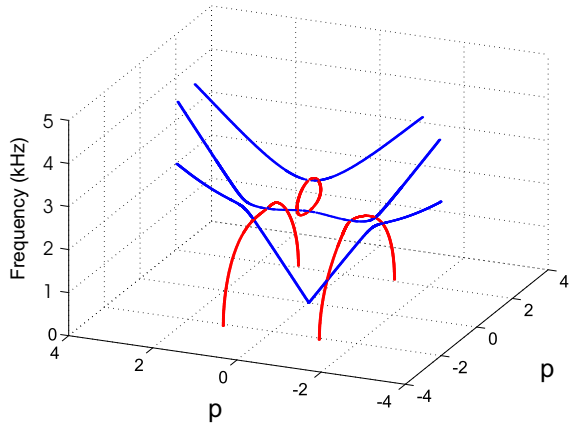

Fig. 7. Simulated plate modes

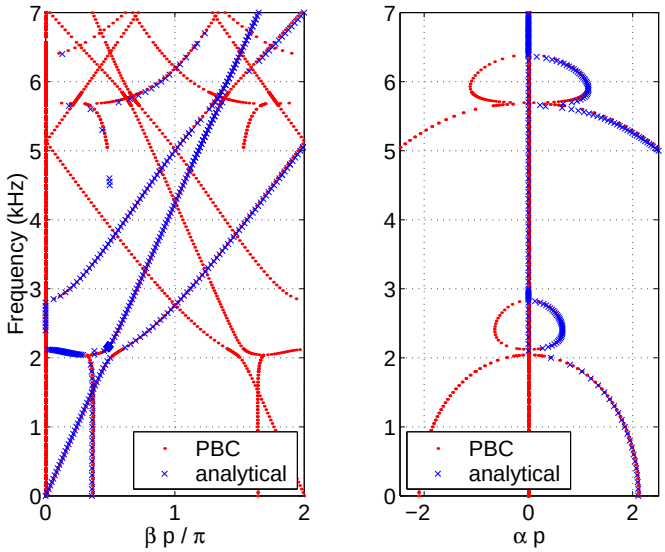

Fig. 8. Quantitative comparison of analytical and simulated results of lamb modes

III. Results

The model illustrated in Fig. 9 has been used for all following calculations.

A. Dispersion Diagram of a Structure on 36° YX-$LiTaO_3$

First, a simulation with aluminum electrodes of 0.2 μm height, a metalization ratio ζ ($\zeta = w_{El}/p$ with w_{El} the electrode width) of 0.7 and a substrate material of 36° YX-$LiTaO_3$ was performed. The material data were taken from [24]. The pitch p was chosen to be 1.33 μm. At this cut of $LiTaO_3$, the displacements of the surface wave do not restrict to the sagittal plane. Therefore, the displacements in all three space directions and the full anisotropy of the material have to be taken into account, although the model itself may be kept two dimensional.

The comparison of the simulated and measured results are shown in Fig. 10. It was not possible to obtain mea-

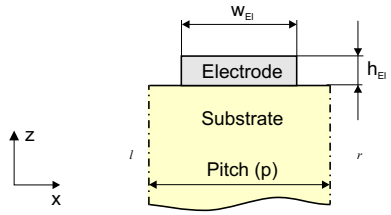

Fig. 9. Model for the simulation of wave propagation in periodic SAW structures

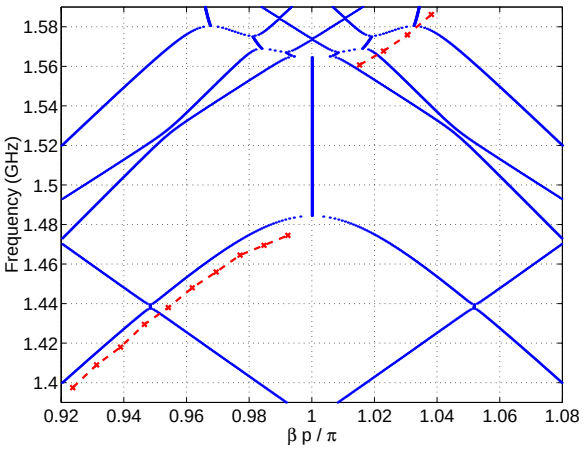

Fig. 10. Comparison of simulated (dots) and measured (crosses) dispersion data

sured results for frequencies in the stopband. Therefore, just the propagation branches of the surface wave can be compared to the simulated results. In Fig. 10, many types of propagation modes can be identified. The one starting at low frequency in the middle of the figure is a Rayleigh mode. In the upper part of the figure, bulk acoustic wave modes can be determined which interact with the surface wave. The interesting mode, which is compared to measured data, is a leaky surface wave (LSAW).

Compared to measured data, the simulation leads to slightly higher stopband edges. This can be explained with the finite simulation domain. With increasing depth of the simulated substrate, the solution converges against the measured results, because the i-th approximated eigenvalue is bounded from below by the i-th exact eigenvalue while Galerkin rules are not violated (e.g. when reduced integration is employed) [2]. Finer meshes lead to larger eigenvalue problems which can't be handled efficiently at the moment.

B. The Stopband Width of a Structure on 37.5° Rotated Quartz as a Function of the Metalization Ratio

The following simulations and measurements have been performed on a substrate of 37.5° rotated quartz with aluminum electrodes. The material constants have been taken from [25]. The height of the electrode h_{El} was fixed to 250 nm, the pitch p at $4\,\mu m$ and the metalization ration ζ has been varied to show the influence of the electrode width on the propagation properties, like stopband edge and stopband width. The substrate height was chosen to be eight pitches.

As an example, the dispersion diagram of a SAW structure with a metalization ration of $\zeta = 0.5$ can be seen in Fig. 11. The measured frequencies are slightly beneath the simulated ones. Again, this can be attributed to the chosen FE grid. This property has been experimentally proofed by simulations with substrate height of only four pitches. In that case, the stopband edges raise additionally 2 MHz at a total stopband width of about 5 MHz.

Various metalization ratios have been examined with our method (see Fig. 12). Measurements are possible only outside the stopband. Therefore, the measured data has been extrapolated to the value $\beta p/\pi = 1$ to obtain the measured stopband width for comparison. The influence of the electrode width on the stopband size can be seen clearly. It is caused mainly by the additional mass loading [14]. As shown in [17], the stopband increases if the reflectivity per electrode gets larger. This is the case when the total mass of the electrode increases.

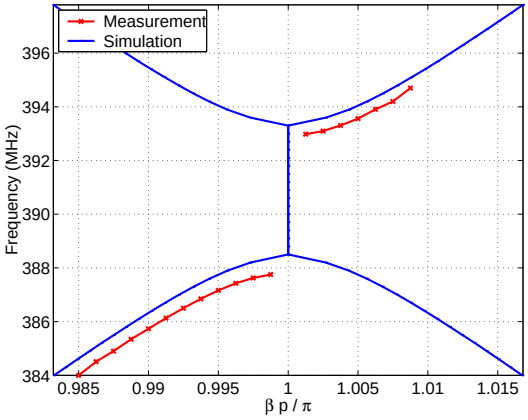

Fig. 11. Exemplary dispersion diagram for $\zeta = 0.5$ of SAW structures on 37.5° rotated quartz

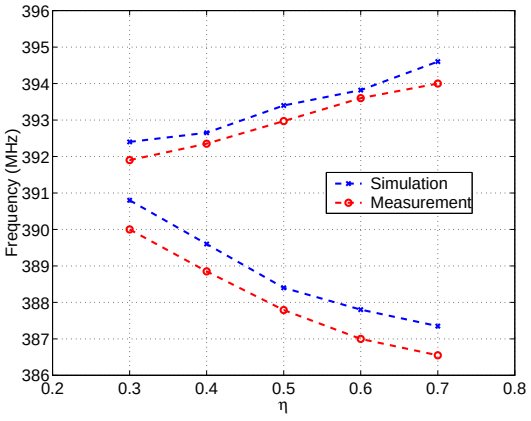

Fig. 12. Stopband edges as a function of metalization ratio ζ of SAW structures on 37.5° rotated quartz (maximum relative error = 2.1‰)

C. Charge Distribution in Electrodes on 37.5° Rotated Quartz

With the same configuration as in the preceeding chapter, simulations of the charge distribution on an electrode have been performed (see Fig. 13). For the calculation of the charge distribution at all electrode edges, the air surrounding the electrode has to be taken into account. In air, the electric potential has to be calculated but the mechanical field may be neglected due to the extremely low mechanical stiffness of the surrounding air. Anyway, the vanishing stress contribution on the free substrate surface must be considered. Especially for materials with low dielectric constants (relative dielectric constants of quartz: $\varepsilon_{r_{xx}} = 4.5$ and $\varepsilon_{r_{zz}} = 4.6$) the surface charge of the electrode-air interfaces has to be taken into account. The charge on these interfaces can be estimated by $1/\varepsilon_r$ times the charge of the electrode-substrate interface. Calculating the total charge at electrodes on a quartz substrate one would make an error of at least 16% by neglecting the charge on the electrode-air interfaces.

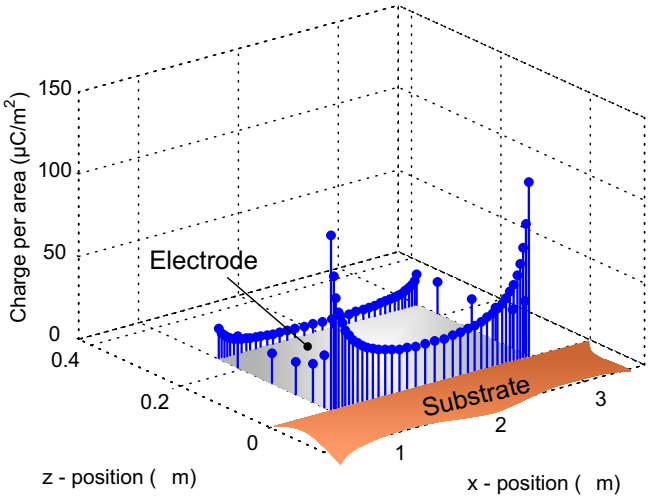

Fig. 13. Charge distribution at an aluminum electrode on 37.5° rotated quartz

D. Calculation of the Input Admittance of a Structure on 36° YX-$LiTaO_3$

A periodically arranged structure on 36° YX-$LiTaO_3$ with a pitch of 1 μm is examined (see Fig. 9). The metalization ratio ζ is fixed to 0.7 and the electrode has a height h_{El} of 200 nm. The substrate material data have been taken from [24] and those of aluminum from [25]. The area above the electrode has not been taken into account because the considered material has a high permittivity ($\varepsilon_r \approx 40$) and therefore, this simplification has not much impact on the simulation results. The depth of the simulation domain has been chosen to three pitches.

To verify the results of the simulation, measured data of a synchronous one-port resonator with 150 IDT fingers and 60 reflector fingers on each side of the IDT has been compared to the simulation. Due to the large amount of IDT and reflector fingers, end effects as a result of the finite length of the structure have a minor influence on the admittance versus frequency curve in the vicinity of the stopband. Therefore, this structure can be used to validate the simulation of the strictly periodically structure to a good approximation.

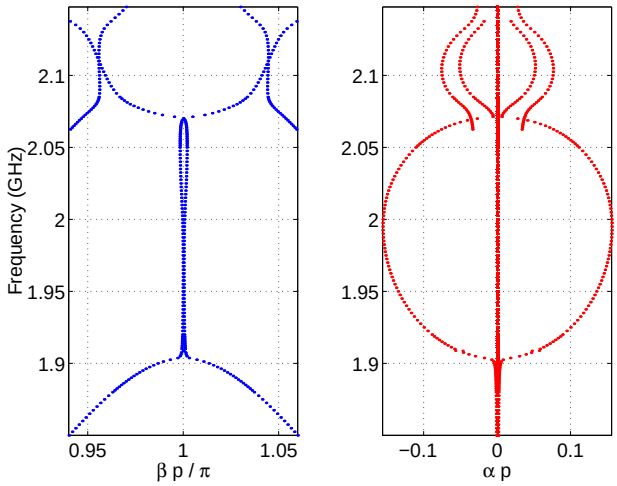

Fig. 14. Simulated propagation constant β and decay constant α

A comparison of the dispersion curve with measured data shows a good agreement of the stopband edge frequencies. In the real part of the admittance plot, they can be figured out as peaks at 1.905 GHz and 2.07 GHz. In the according simulation in Fig. 15, the upper stopband edge is not visible, because this is a result of a finite-length structure.

The values of the originally simulated admittance at the resonance frequencies have been slightly larger than those of the measurement. This is a result of the electrical resistance of the electrode fingers and other small resistances which appear in measurements, e.g. the contact resistance between measurement tips and bonding pads. This series resistance has been calculated to 0.3 Ω and incorporated into the simulated results.

Comparing the original simulated and measured data of the admittance, a small frequency shift of 5.5 MHz (corresponding to 3‰) could be discovered. This is again an artifact of the chosen FE grid. In addition, for the imaginary part of the admittance $\Im(Y)$, a shift to smaller values could be figured out. Possible explanations for this difference are a small spurious capacitance parallel to the measured device or small fabrication tolerances. These influences will be investigated in more detail in the near future. To allow a better comparison of measured and simulated data and to account for the aforementioned effects, a parallel capacitance of 2 pF has been incorporated into the simulated data and the simulated curve has been shifted in frequency by 5.5 MHz towards zero.

IV. Conclusion

Two different algorithms for the calculation of waves in periodic piezoelectric structures have been introduced.

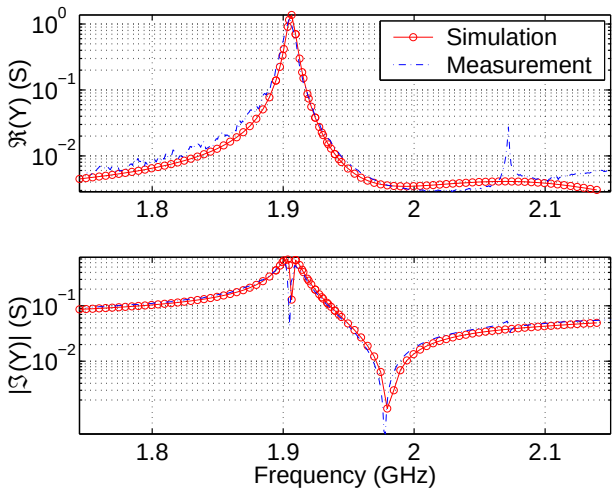

Fig. 15. Real ($\Re$(Y)) and imaginary ($\Im$(Y)) part of measured and simulated admittance (Simulation with frequency shift of -5.5 MHz, including a series resistance of 0.3 Ω and a parallel capacitance of 2 pF)

They are based on the finite element method (FEM), which allows the simulation of waves on any piezoelectric substrates, with arbitrary electrode shapes or even additional electrode cover layers.

The resulting eigenvalue problems is used to calculate the dispersion relation of the propagating waves, including the damping coefficient. By reformulating the system, it is possible to calculate the charge distribution on an electrode at given electric excitation.

Several simulation results on 36°YX-$LiTaO_3$ and 37.5° rotated quartz have been compared to measurements. They show that the newly developed methods can be used for the precise prediction of wave propagation parameters and input admittances.

References

[1] K.J. Bathe, *Finite Element Procedures*, Prentice-Hall, New Jersey, 1996.

[2] T.J.R. Hughes, *The Finite Element Method*, Prentice-Hall, New Jersey, 1 edition, 1987.

[3] O.C. Zienkiewicz, *The Finite Element Method*, McGraw-Hill, New York, 4 edition, 1994.

[4] M. Jung and U. Langer, *Methode der finiten Elemente für Ingenieure: Eine Einführung in die numerischen Grundlagen und Computersimulation*, B.G. Teubner GmbH, Stuttgart-Leipzig-Wiesbaden, 2001.

[5] P. Ciarlet, *The Finite Element Method for Elliptic Problems*, North-Holland Publishing Company, Amsterdam-New York-Oxford, 1978.

[6] Susanne C. Brenner and Ridgway L. Scott, *The Mathematical Theory of Finite Element Methods*, Springer, New York, 1994.

[7] David P. Morgan, *Surface-Wave Devices for Signal Processing*, vol. 19 of *Studies in Electrical and Electronic Engineering*, Elsevier, 1991.

[8] Colin K. Campbell, *Surface Acoustic Wave Devices*, Applications of Modern Acoustics. Acacdemic Press, San Diego, 1998.

[9] Reinhard Lerch, "Analyse hochfrequenter akustischer Felder in Oberflächenwellenfilter-Komponenten," in *AEÜ*, 1990, vol. 44, pp. 317–327.

[10] Ruth M. Orris and M. Petyt, "A Finite Element Study of Harmonic Wave Propagation in Periodic Structures," *Journal of Sound and Vibration*, vol. 33, no. 2, pp. 223–236, 1974.

[11] Philippe Langlet, Anne-Christine Hladky-Hennion, and Jean-Noël Decarpigny, "Analysis of the Propagation of Plane Acoustic Waves in Passive Periodic Materials Using the Finite Element Method," *Journal of the Acoustic Society of America*, vol. 98, no. 5, pp. 2792–2800, 1995.

[12] M. Åberg and P. Gudmundson, "The Usage of Standard Finite Element Codes for Computation of Dispersion Relations in Materials with Periodic Microstructure," *Journal of the Acoustic Society of America*, vol. 102, no. 4, pp. 2007–2013, 1997.

[13] A. C. Hennion, R. Bosssut, and J. N. Decarpigny, "Analysis of the Scattering of a Plane Acoustic Wave by a Periodic Elastic Structure Using the Finite Element Method: Application to Compliant Tube Gratings," *Journal of the Acoustic Society of America*, vol. 87, no. 5, pp. 1861–1870, 1990.

[14] C. Dunnrowicz, F. Sandy, and T. Parker, "Reflection of Surface Waves from Periodic Discontinuities," in *IEEE Ultrasonic Symposium Proceedings*, 1976, pp. 386–390.

[15] Markus Buchner, Werner Ruile, Anselm Dietz, and Roland Dill, "FEM Analysis of the Reflection Coefficient of SAWs in an Infinite Periodic Array," in *IEEE Ultrasonics Symposium Proceedings*, 1991, pp. 371–375.

[16] Yook-Kong Yong, "Analysis of Periodic Structures for BAW and SAW Resonators," in *IEEE Ultrasonics Symposium Proceedings*, 2001, to be published.

[17] Dong-Pei Chen and Herman A. Haus, "Analysis of Metal-Strip SAW Gratings and Transducers," *IEEE Transactions on Sonics and Ultrasonics*, vol. 32, no. 3, pp. 395–408, 1985.

[18] Reinhard Lerch, "Simulation of Piezoelectric Devices by Two- and Three-Dimensional Finite Elements," *IEEE Trans. Ultrasonics, Ferroelectrics and Frequency Control*, vol. 37, no. 3, pp. 233–247, 1990.

[19] A. Y. Leung, "Inverse Iteration for the Quadratic Eigenvalue Problem," *Journal of Sound and Vibration*, vol. 124, no. 2, pp. 247–267, 1988.

[20] C. Rajakumar, "Lanczos Algorithm for the Quadratic Eigenvalue Problem in Engineering Applications," *Computer Methods in Applied Mechanics and Engineering*, vol. 105, pp. 1–22, 1993.

[21] D. Afolabi, "Linearization of the Quadratic Eigenvalue Problem," *Computers and Structures*, vol. 26, no. 6, pp. 1039–1040, 1987.

[22] E. Anderson, Z. Bai, C. Bischof, S. Blackford, J. Demmel, J. Dongarra, J. Du Croz, A. Greenbaum, S. Hammarling, A. McKenney, and D. Sorensen, Eds., *LAPACK Users' Guide*, SIAM, 3 edition, 1999.

[23] B. A. Auld, *Acoustic Fields and Waves in Solids*, vol. 2, Krieger Publishing Company, Inc., Florida, 2 edition, 1990.

[24] G. Kovacs, M. Anhorn, H. E. Engan, G. Visintini, and C. C. W. Ruppel, "Improved Material Constants for $LiNbO_3$ and $LiTaO_3$," in *IEEE Ultrasonics Symposium Proceedings*, 1990, pp. 435–438.

[25] B. A. Auld, *Acoustic Fields and Waves in Solids*, vol. 1, Krieger Publishing Company, Inc., Florida, 2 edition, 1990.